



Synergistic hydroxyl radical formation, system X_C- inhibition and heat shock protein crosslinking tango in ferrotherapy: A prove-of-concept study of “sword and shield” theory



Li Xie^a, Wenjie Chen^a, Qifang Chen^a, Yang Jiang^a, Erqun Song^a, Xiaokang Zhu^{a,**}, Yang Song^{b,*}

^a Key Laboratory of Luminescence Analysis and Molecular Sensing, Ministry of Education, College of Pharmaceutical Sciences, Southwest University, 2 Tiansheng Rd, Beibei District, Chongqing, 400715, China

^b State Key Laboratory of Environmental Chemistry and Ecotoxicology, Research Center for Eco-Environmental Sciences, Chinese Academy of Sciences, 18 Shuangqing Rd, Haidian District, Beijing, 100085, China

ARTICLE INFO

Keywords:
Ferroptosis
ROS
LPO
System X_C
HSP

ABSTRACT

Ferroptosis provide new insights into designing nanomedicines for enhanced cancer therapy; however, its anti-tumor efficacy is relatively low, mainly due to self-protective mechanism of cancer cells, e.g., heat shock protein (HSP) overexpression. Since HSPs can be modified/inhibited by lipid peroxidation (LPO) ending products, we construct a nanoplatfrom, namely MPDA@Fe₃O₄-Era, to amplify intracellular reactive oxygen species (ROS) and LPO for synergistic ferrotherapy. Upon tumor acidic microenvironment and local near-infrared stimuli, this nanoplatfrom releases Fe₃O₄ and reacts with intracellular hydrogen peroxide (H₂O₂) to promote Fenton reaction, and yields significant intracellular ROS (specifically hydroxyl radical, •OH) and LPO. In turn, LPO ending products crosslink HSPs to destroy self-preservation pathways of cancer cells to enhance anticancer effect. Meanwhile, the released erastin inhibits system X_C signal pathway to depletes glutathione. Fe₃O₄ loading further provides magnetic resonance imaging T2-weighted signal to guide anti-tumor treatment. Together, this nanoplatfrom not only provides •OH (as a “sword” to attack tumor cells), but also inhibits system X_C signal pathway and crosslinks HSP (break down the “shield” of tumor cells) to maximize synergistic ferro-therapeutic effect. MPDA@Fe₃O₄-Era plus laser irradiation possessed highly efficient tumor suppression with magnified the levels of •OH and inactive glutathione peroxidase 4 (GPX4), which can promote the development of precise cooperative cancer therapy.

1. Introduction

Ferroptosis, a new form of iron-dependent cell death, closely relates to intracellular accumulation of reactive oxygen species (ROS) and lipid peroxidation (LPO), which leads to membrane destruction, to membrane pores opening and membrane rupture [1,2]. Ferroptosis is recognized as a promising strategy in overcoming resistance to chemotherapy in cancer; however, mounting evidence has shown that cancer cells are able to resist ferroptotic stress through regulating iron metabolism, anti-oxidative systems, and lipid metabolism and etc [3]. Therefore, it is urgent to reveal the underlying mechanisms associated with ferroptosis resistance.

Ferroptosis mainly occurs with oxidized glutathione (GSH) and the breakdown of system X_C/glutathione peroxidase 4 (GPX4) signal pathway [4,5]. In addition, ferroptotic insult yields uncontrolled peroxidation of phospholipids containing polyunsaturated fatty acids within the cell membranes [6,7]. However, heat shock proteins (HSPs) repair cell through a variety of stress-related pathways and protect cells from ferroptosis, which leads to resistance [8,9]. Mechanistically, HSPs bound GPX4 and block its degradation and subsequent LPO [8].

Intracellular iron contributes to ferroptosis through producing ROS by Fenton reaction. Transferrin (TF) transport two Fe³⁺ to transferrin receptor 1 (TFR1) and form TF-(Fe³⁺)²-TFR1 compounds to enter lysosomes in the cells [10]. After reduction, Fe²⁺ was stored in a labile iron

* Corresponding author. Key Laboratory of Luminescence Analysis and Molecular Sensing, Ministry of Education, College of Pharmaceutical Sciences, Southwest University, 2 Tiansheng Rd, Beibei District, Chongqing, 400715, China.

** Corresponding author.

E-mail addresses: zxk@swu.edu.cn (X. Zhu), yangsong@rcees.ac.cn (Y. Song).

<https://doi.org/10.1016/j.mtbio.2022.100353>

Received 20 April 2022; Received in revised form 23 June 2022; Accepted 4 July 2022

Available online 7 July 2022

2590-0064/© 2022 The Authors. Published by Elsevier Ltd. This is an open access article under the CC BY-NC-ND license (<http://creativecommons.org/licenses/by-nc-nd/4.0/>).

pool for Fenton reaction, while excessive Fe^{3+} was stored in ferritin [11]. Moreover, iron metabolism *in vivo* is precisely regulated by ferroportin1 (FPN1). FPN1, an iron channel, can transport iron from cells to extracellular and circulatory systems to reduce iron overload and furtherly maintain intracellular iron homeostasis [12]. However, HSPs was proved to suppress TRF1 expression to reduce intracellular iron concentration [9]. In this regard, HSPs was considered as the negative regulator of ferroptosis, and HSPs inhibition increases the efficiency of ferroptosis. It has been reported that the primary amines of HSPs could be cross-linked by ROS or LPO ending products [13,14].

In this study, we reported a multifunctional theranostic nanoplat-form, namely MPDA@ Fe_3O_4 -Era, with synergistic effects to against ferroptosis resistance. Erastin (Era) and Fe_3O_4 nanoparticles (NPs) were loaded into the mesopores or onto the surface of mesoporous polydopamine (MPDA) for the fabrication of multifunctional MPDA@ Fe_3O_4 -Era. Upon acidic tumor microenvironment and local near-infrared stimuli, this nanoplat-form releases Fe_3O_4 and then triggered Fenton reaction to yield hydroxyl radical ($\cdot\text{OH}$). Meanwhile, endowed Era suppressed system $\text{Xc}^-/\text{GPX4}$ signal, which further elevates LPO accumulation. Spontaneously, excess ROS and downstream LPO ending products block HSPs signal. In addition, Fe_3O_4 loading provides magnetic resonance imaging (MRI) T2-weighted signal to guide anti-tumor treatment. Thus, the significant therapeutic effect could be achieved due to synergistic ferroptosis.

2. Experimental section

2.1. Chemicals

All reagents were commercially available and utilized without further purification. Dopamine hydrochloride ($\text{DA}\cdot\text{HCl}$), ammonia ($\text{NH}_3\cdot\text{H}_2\text{O}$), Pluronic F127, 1,3,5-trimethylbenzene (TMB), ethanol, acetone, defiprone (DFP), ferostatin-1 (Fer-1), Eugenol, rhodamine B (Rh B) and Era were bought from Aladdin Biochemical Technology Co., LTD (Shanghai, China). VER155008 was bought from Selleck Chemical Co., LTD (Shanghai, China). DAPI, antibodies against TFR and HSP70 were supplied by Wanlei Biotechnology Co., Ltd (Shenyang, China). 2',7'-Dichlorodihydrofluorescein diacetate (DCFH-DA) and hydrogen 11-(5,5-difluoro-7-((1E,3E)-4-phenylbuta-1,3-dien-1-yl)-5H-514,614-dipyrrolo [1,2-c2',1'-f][1,3,2] diazaborinin-3-yl) undecanoate (C11BODIPY) were bought from Sigma-Aldrich Co., LLC (Shanghai, China). Calcein-AM and PI double-staining probe, JC-1 probe were supplied by Yeasen Biotechnology (Shanghai, China). Antibodies against acyl-CoA synthetase long chain family member 4 (ACSL4), solute carrier family 7-member 11 (SLC7A11), FPN and GPX4 were purchased from Santa Cruz Biotechnology (Santa Cruz, CA). Antibodies against ferritin heavy chain 1 (FTH1) were purchased from Bioss Biotechnology Co., Ltd (Beijing, China). Real-time polymerase chain reaction (RT-qPCR) amplification primers for GPX4, ACSL4 and SLC7A11 were synthesized by Sangon Biotech Co., Ltd (Shanghai, China). Malondialdehyde (MDA), iron concentration and GSH kits were purchased from Jiancheng Biological Engineering Research Institute Co., Ltd (Nanjing, China). ATP kit was purchased from Solarbio Science & Technology Co., Ltd (Beijing, China).

2.2. Characterizations

The structure and morphology of NPs were characterized by transmission electron microscopy (TEM, HT7800, HITACHI) and field emission scanning electron microscope (FESEM, JSM-7800 F, JEOL). The hydrodynamic particle size distribution and zeta potential of NPs were determined by dynamic light scattering (DLS, ZEN3700, Malvern). Erastin and Fe_3O_4 loading were analyzed by an ultraviolet spectrophotometer (UV-Vis, UV-2450, BIO-RAD) and inductively coupled plasma optical emission spectrometer (ICP-OES, AVIOTM 200, Perkin Elmer), respectively. The compositional changes were analyzed by infrared spectrometer (IR, Prestige-21, Shimadzu).

2.3. Synthesis of MPDA NPs

MPDA NPs were prepared according to the previously reported method with slight modifications [15]. Briefly, 0.36 g of Pluronic F127 and 0.36 g of TMB were dissolved in mixture solution of H_2O (75 mL) and ethanol (40 mL) and stirred at room temperature for 30 min. Then, 2 mL of ammonia solution (NH_4OH , 28–30%, w/w) was added to the above mixture and stirred for another 30 min. Meanwhile, $\text{DA}\cdot\text{HCl}$ (0.5 g) dissolved into 15 mL deionized water was slowly dropped into the mixture and stirred at room temperature for 24 h. The obtained particles were separated by centrifugation at 10,000 g for 10 min. The sediments were placed in a mixed solution of ethanol and acetone (2:1, v/v) and then sonicated (three times, 30 min per time) to remove the template (F127 and TMB).

2.4. Synthesis of MPDA@ Fe_3O_4 -Era

Briefly, MPDA (0.8 mg) was added into 1 mL DMSO solution contained different weight of Era (0.8, 0.6, 0.4, 0.2 mg). Then, the oleic acid coated Fe_3O_4 NPs (0.2 mg) solution was added and the reaction mixture was continuously stirred at room temperature for 24 h. The MPDA@ Fe_3O_4 -Era was purified via dialyzing (MWCO: 1000 Da) with double instilled water for 24 h.

2.5. In vitro drug load and release study

After synthesis of MPDA@ Fe_3O_4 -Era, we detected the loading concentrations of Era and Fe_3O_4 in MPDA@ Fe_3O_4 -Era as follows. Consistently, the encapsulation efficiency (EE) of the drug was calculated using the equation (mg/mg): $\text{EE} (\%) = (\text{mass of drug in MPDA@Fe}_3\text{O}_4\text{-Era} / \text{mass of total drug}) \times 100\%$. Similarly, the loading capacity (LC) of the drug was calculated as follows (mg/mg): $\text{LC} (\%) = (\text{mass of drug in MPDA@Fe}_3\text{O}_4\text{-Era} / \text{mass of MPDA@Fe}_3\text{O}_4\text{-Era}) \times 100\%$.

The influence of near-infrared (NIR) laser and pH value on the drug release behavior was evaluated as follows. MPDA@ Fe_3O_4 -Era (160 mg/mL) were contained in a dialysis bag (MWCO: 1000 Da) and immersed in phosphate buffers (PBS) with different pH values (pH 5.0, 6.5 or 7.4). MPDA@ Fe_3O_4 -Era was irradiated with an 808 nm NIR laser at a power density of 1.5 W cm^{-2} for 5 min, at different time (0, 0.5, 1, 2, 4, 8, 16 h). 1 mL solution was then collected after different treatments and 1 mL buffer solution was supplied. The released Era was analyzed by UV-Vis spectrometer, while the release of Fe was measured by ICP-OES.

2.6. In vitro photothermal properties study

To investigate the photothermal property, MPDA@ Fe_3O_4 -Era was dissolved in PBS at different concentrations (0, 125, 250, 500 $\mu\text{g mL}^{-1}$) and then exposed to 808 nm laser with different power densities (0.5, 1.0, 1.5, 2.0 W cm^{-2}) for 11 min. Meanwhile, a numerical control thermometer was used to record the temperature change at each 30 s. The photothermal conversion efficiency of MPDA@ Fe_3O_4 -Era was calculated according to previously reported method [16].

$$\eta = \frac{hS(T_{\max} - T_{\text{surr}}) - Q_0}{I(1 - 10^{-A808})} = \frac{hS(T_{\max} - T_{\text{surr}}) - hS(T_{\max, \text{water}} - T_{\text{surr}})}{I(1 - 10^{-A808})}$$

$$\theta = \frac{\Delta T}{\Delta T_{\max}} = \frac{T - T_{\text{surr}}}{T_{\max} - T_{\text{surr}}}$$

$$\tau_s = \frac{m_d c_d}{hS}$$

where h is the heat transfer coefficient, S is the surface area of the sample container. T_{\max} is the steady-state maximum temperature of the hydrogel. $T_{\max, \text{water}}$ is the steady-state maximum temperature of the water. T_{surr} is the ambient room temperature. Q_0 is the background energy input

by the solvent and the sample container. I represent the laser current. A808 is the absorbance of MPDA@Fe₃O₄-Era at 808 nm.

To assess the photostability of photothermal, MPDA@Fe₃O₄-Era was firstly dissolved in PBS at 250 µg mL⁻¹ and periodically treated with NIR laser (808 nm, 1.5 W cm⁻², 11 min) followed by cooling down for 5 times, and the change of temperature was recorded by a numerical control thermometer.

2.7. In vitro magnetic resonance (MR) imaging

MR signals of different concentrations of MPDA@Fe₃O₄-Era (0, 54, 108, 216, 431 and 862 µM) in the 1.5 mL epoxy resin tubes were attached at the bottom of the detector and measured by magnetic resonance imaging analyzer (MesoMR23-060H-I, Niumag Corporation).

2.8. Cellular culture

The murine breast cancer 4T1 cell line was purchased from Army Medical University. Cells were cultured in Dulbecco's modified eagle medium (DMEM) supplemented with 10% fetal bovine serum (FBS) and 1% penicillin–streptomycin at 37 °C with 5% CO₂.

2.9. Cellular uptake

MPDA@Fe₃O₄-Era was modified by Rh B for cell imaging. 4T1 cells were seeded 12 well plate (1 × 10⁴ cell per well) and incubated for 24 h. Then, Rh B labeled MPDA@Fe₃O₄-Era (MPDA: 100 µg mL⁻¹) were added to the incubation media (DMEM plus 10% FBS) at different times (0, 0.5, 1.0, 1.5, 2.0 h). The cells were washed with PBS for three times to remove the residual drug. The cellular internalization behavior of the MPDA@Fe₃O₄-Era was investigated by FCM (FACS Melody, Becton Dickinson).

To visualize the cellular uptake, 4T1 cells were co-incubated with Rh B labeled MPDA@Fe₃O₄-Era at a concentration of 100 µg mL⁻¹ MPDA. After co-culture for different time (0.5, 1.0, 1.5 and 2.0 h), 4T1 cells were stained with DAPI for 10 min and washed with PBS for three times. After that, cells were imaged under a confocal laser scanning microscope (CLSM, N-SIM E, Nikon).

2.10. In vitro cytotoxicity test

For cell viability study, 4T1 cells were seeded in 96-well plates (4 × 10³ cell per well) and cultured for 24 h 100 µL of MPDA@Fe₃O₄-Era (0, 20, 40, 80, 160, 320 µg mL⁻¹) solutions were added into each well. A fresh DMEM medium was used as the control. Then the cells were incubated for another 24 h and replaced with fresh culture media. 10 µL of CCK8 solution was added to the fresh medium. After 4 h of incubation, the absorbance was measured at 450 nm by a microplate reader (ELX-800, BIO-RAD).

To explore the photothermal therapy (PTT) therapeutic, 4T1 cells were pretreated with MPDA@Fe₃O₄-Era (an equivalent concentration of 100 µg mL⁻¹ MPDA) for 2 h. Subsequently, the cells were irradiated by various power densities of 808 nm NIR laser (0.5, 1.0, 1.5 W cm⁻²) for 6 min, and then cultured for another 24 h. Finally, the cell viability was measured by CCK8 according to the manufactory's instruction (Yeasen Biotechnology).

For the live/dead fluorescence staining study, 4T1 cells were pretreated with MPDA, MPDA@Fe₃O₄, MPDA@Era, MPDA@Fe₃O₄-Era and MPDA@Fe₃O₄-Era plus laser at an equivalent concentration of 100 µg mL⁻¹ MPDA. Laser represents the group was exposed to an 808 nm laser (1.5 W cm⁻², 6 min) after incubation for 2 h. Fresh DMEM medium was used as the control. Then, cells were incubated for 24 h. After staining with calcein-AM/PI, cells were observed using CLSM.

2.11. Detection of the ROS and LPO levels

Briefly, 4T1 cells were seeded in confocal dish (1 × 10⁴ cell per well)

and cultured for 24 h 4T1 cells were pretreated with MPDA, MPDA@Fe₃O₄, MPDA@Era, MPDA@Fe₃O₄-Era and MPDA@Fe₃O₄-Era plus laser at an equivalent concentration of 100 µg mL⁻¹ MPDA. Laser represents the group was exposed to an 808 nm laser (1.5 W cm⁻², 6 min). After 6 h, cell suspensions were collected, and incubated with the DCFH-DA and C11BODIPY probes for 30 min to detect the levels of ROS and LPO ending products via CLSM, respectively. The fluorescence emissions images of DCFH-DA and C11BODIPY through single green channel were recorded by CLSM.

2.12. Evaluation of mitochondrial membrane potential (ΔΨ_m, MMP)

Briefly, 4T1 cells were seeded in confocal dish (1 × 10⁴ cell per well) and cultured for 24 h 4T1 cells were pretreated with MPDA, MPDA@Fe₃O₄, MPDA@Era, MPDA@Fe₃O₄-Era and MPDA@Fe₃O₄-Era plus laser at an equivalent concentration of 100 µg mL⁻¹ MPDA. Laser represents the group was exposed to an 808 nm laser (1.5 W cm⁻², 6 min). After 6 h, cell suspensions were collected, and incubated with JC-1 for 15 min. Thereafter, the extra probes were removed by washing with PBS. Finally, the relative green and red fluorescence intensities of cells were recorded by CLSM.

2.1.3. ATP assay

Briefly, 4T1 cells were seeded in 6-well plates (8 × 10⁴ cell per well) and cultured for 24 h 4T1 cells were pretreated with MPDA, MPDA@Fe₃O₄, MPDA@Era, MPDA@Fe₃O₄-Era and MPDA@Fe₃O₄-Era plus laser at an equivalent concentration of 100 µg mL⁻¹ MPDA. Laser represents the group was exposed to an 808 nm laser (1.5 W cm⁻², 6 min). After 6 h, Cell lysis solutions were harvested, and protein concentrations were determined by the bicinchoninic acid (BCA) protein concentration determination method. Total ATP levels were measured by a commercial ATP kit according to the manufacturer's instructions (Jiancheng Biological Engineering Research Institute Co., LTD).

2.14. In vitro western blotting

4T1 cells were seeded in 6-well plates (8 × 10⁴ cell per well) and cultured for 24 h Cells were treated with MPDA@Fe₃O₄, MPDA@Era, MPDA@Fe₃O₄-Era, MPDA@Fe₃O₄-Era + Glu, MPDA@Fe₃O₄-Era + Cys and MPDA@Fe₃O₄-Era + DFP at an equivalent concentration of 100 µg mL⁻¹ MPDA (Glu: 2 mM; Cys: 2 mM; DFP: 100 µM) for another 24 h. The cells lysates were collected by centrifugation for 10 min at 14,000 g under 4 °C. The cell lysates containing the loading buffer were analyzed by electrophoresis on 12.5% denaturing polyacrylamide gels to detect the levels of ACSL4, SLC7A11, GPX4, FPN1, TFR and FTH1.

To explore the synergistic ferroptosis and photothermal effect, 4T1 cells were seeded in 6-well plates (8 × 10⁴ cell per well) and cultured for 24 h 4T1 cells were pretreated with control plus laser, MPDA plus laser, MPDA@Fe₃O₄ plus laser, MPDA@Era plus laser and MPDA@Fe₃O₄-Era plus laser at an equivalent concentration of 100 µg mL⁻¹ MPDA. Besides, 4T1 cells were pretreated with control plus laser, MPDA plus laser, MPDA + VER155008 plus laser, MPDA@Fe₃O₄-Era plus laser, MPDA@Fe₃O₄-Era + Eugenol plus laser and MPDA@Fe₃O₄-Era + Fer-1 plus laser at an equivalent concentration of 100 µg mL⁻¹ MPDA (VER155008: 10 µM; Eugenol: 100 µM; Fer-1: 20 µM). Laser represents the groups were exposed to an 808 nm laser (1.5 W cm⁻², 6 min) after incubation for 2 h. After 4 h, the cell lysates were collected by centrifugation for 10 min at 14,000 g under 4 °C. The cell lysates containing the loading buffer were analyzed by electrophoresis on 12.5% denaturing polyacrylamide gels to detect the levels of HSP 70 proteins.

2.15. RT-qPCR

Briefly, total RNA was extracted with a high purity RNA extraction kit as described in the manufacturer's instruction (TianGen Biochemical

Technology Co., LTD). The purified RNA was reverse transcribed into cDNA with the first stand cDNA synthesis kit. Subsequently, cDNA was used for DNA amplification to perform RT-qPCR analysis using the LightCycler 96 instrument protocol. Finally, 40 cycles of PCR were completed at 60 °C for 90 min. The mRNA expression levels of GPX4, ACSL4 and SLC7A11 were determined by the $2^{-\Delta\Delta Ct}$ method. The sequence of primers for the above genes was shown in Table S1.

2.16. GSH and MDA assay

Briefly, 4T1 cells were seeded in 6-well plates (8×10^4 cell per well) and cultured for 24 h. 4T1 cells were pretreated with MPDA@Fe₃O₄, MPDA@Era, MPDA@Fe₃O₄-Era, MPDA@Fe₃O₄-Era plus Glu and MPDA@Fe₃O₄-Era plus Cys at an equivalent concentration of 100 $\mu\text{g mL}^{-1}$ MPDA (Glu: 2 mM; Cys: 2 mM). After 24 h, Cell lysis solutions were harvested, and protein concentrations were determined by BCA protein concentration determination method. Total GSH was measured by a commercial GSH kit according to the manufacturer's instructions (Jiancheng Biological Engineering Research Institute Co., LTD). MDA level was measured by a commercial MDA kit according to the manufacturer's instruction (Jiancheng Biological Engineering Research Institute Co., LTD).

2.17. Iron concentration assay

Briefly, 4T1 cells were pretreated with MPDA@Fe₃O₄, MPDA@Era, MPDA@Fe₃O₄-Era and MPDA@Fe₃O₄-Era plus DFP at an equivalent concentration of 100 $\mu\text{g mL}^{-1}$ MPDA (DFP: 100 μM). After 24 h, cell lysis solutions were harvested, and protein concentrations were determined by BCA protein concentration determination method. Total iron concentration levels were measured by a commercial total tissue iron concentration kit according to the manufacturer's instruction (Solarbio Science & Technology Co., Ltd).

2.18. Animal handling

Female BALB/c mice (6–8 weeks) were purchased from Teng Xin Technology (Chongqing, China). All animal experiments were conducted with an approval no. IACUC-20210514-03 based on the guidelines of the Institutional Animal Care and Use Committee of Southwest University and the National Institutes of Health guidelines for laboratory animals. To establish the tumor models, all BALB/c female mice were subcutaneously inoculated with 100 μL of cell culture medium with 4T1 cells (5×10^6 per mL) [17]. After the tumor volume reached 80–100 mm³, mice were used for tumor imaging and therapy.

2.19. In vivo real-time fluorescence imaging, MRI and thermal imaging

Sulfo-cyanine5 carboxylic acid (Cy5) was modified onto MPDA@Fe₃O₄-Era to endow the capacity of fluorescence imaging *in vivo*. 1 mg Cy5 was added to the 2 mg MPDA@Fe₃O₄-Era solution in DMSO and stirred overnight. The excessive Cy5 was removed by dialysis (MWCO: 15,000 Da) for 24 h. Cy5-labeled MPDA@Fe₃O₄-Era were obtained after washed with PBS.

4T1 tumor-bearing mice were anesthetized and injected 10 mg kg⁻¹ Cy5-labeled MPDA@Fe₃O₄-Era intravenously through the tail vein. Fluorescent images were acquired at 3, 6, 12 and 24 h by using an *in vivo* imaging system (NEWTON 7.0, Vilber Lourmat). After 24 h post injection of Cy5-labeled MPDA@Fe₃O₄-Era, mice were euthanized to observe *ex vivo* biodistribution. Tumors, heart, liver, spleen, lung and kidney were collected to observe the fluorescence images.

For *in vivo* MRI, 4T1 tumor-bearing mice were anesthetized and injected MPDA@Fe₃O₄-Era and Fe₃O₄ NPs intravenously through tail vein (2 mg kg⁻¹ Fe₃O₄). MRI was acquired at 3, 6, 12 and 24 h by using an *in vivo* imaging system (MesoMR23-060H-I, Niumag Corporation).

For *in vivo* thermal imaging, 4T1 tumor-bearing mice were

anesthetized and injected 8 mg kg⁻¹ MPDA@Fe₃O₄-Era intravenously through the tail vein. After 12 h, thermal imaging was acquired for 808 nm, 1.5 W cm⁻², 6 min by using a thermal imager (E8, Fotric). A fresh PBS medium was injected into the 4T1 tumor-bearing mice as the control.

2.20. In vivo anti-cancer activity

After the tumor volume reached 80–100 mm³, all tumor-bearing BALB/c mice were randomly assigned to 6 groups (n = 5): PBS, MPDA, MPDA@Fe₃O₄, MPDA@Era, MPDA@Fe₃O₄-Era and MPDA@Fe₃O₄-Era plus laser (808 nm, 1.5 W cm⁻², 6 min) at an equivalent MPDA concentration of 20 mg kg⁻¹. Afterwards, tumor sizes and body weights of mice were monitored every day during the 14 days treatment process. The tumor volume was calculated as follows: $V_{\text{tumor}} = (\text{tumor length}) \times (\text{tumor width})^2/2$. On 14th day, the serum of all groups was collected. The mice in various treatments were euthanized. Then, their tumors and major organs including heart, liver, spleen, lung and kidney were collected for subsequent analysis. The serum was collected to measure the levels of ALT, BUN, ALB, and nine blood routine indexes including WBC count, RBC count, Lymph percentage, Mon percentage, Gran percentage, HCT, RDW, PCT, PLT count. Major organs were stained with hematoxylin and eosin (H&E) by a commercial H&E staining kit according to the manufacturer's instructions (Wuhan Servicebio Technology Co., LTD), and tumors were stained with GPX4, HSP70, LPO and H&E by a commercial immunofluorescence staining kit according to the manufacturer's instructions (Wuhan Servicebio Technology Co., LTD).

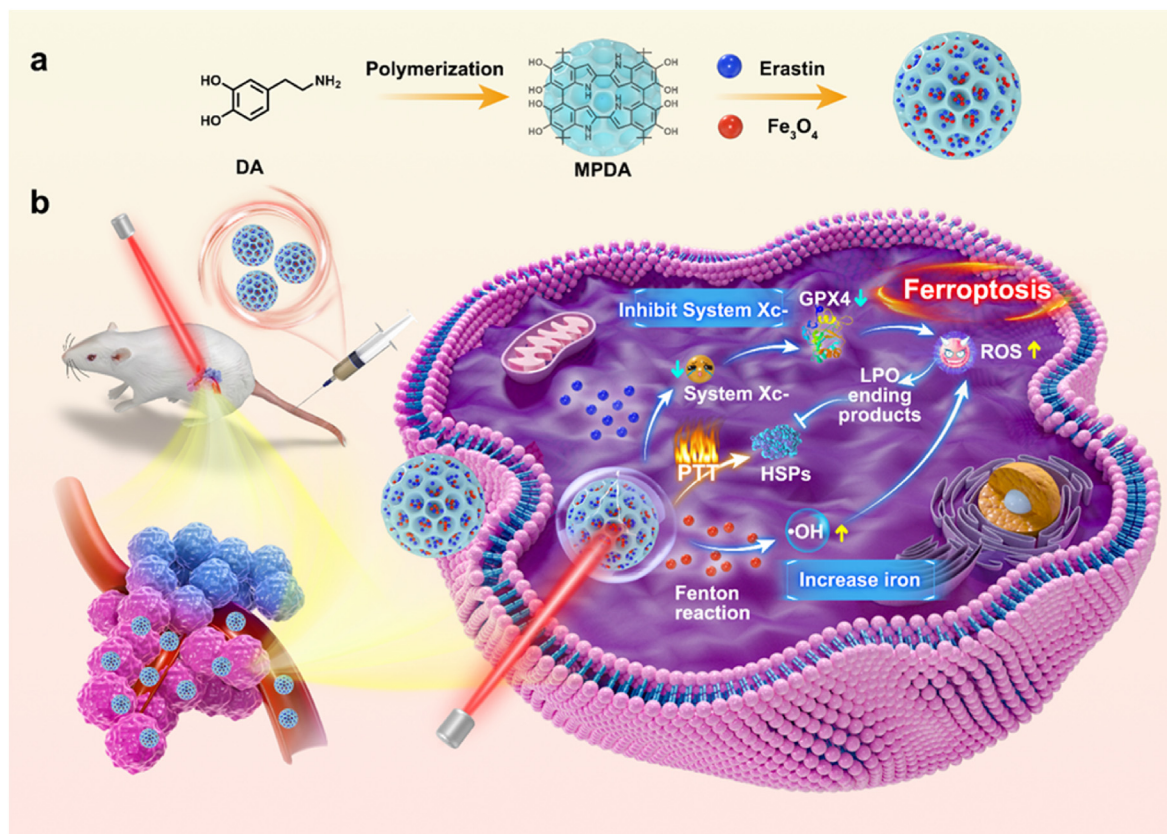
2.21. Statistical analysis

Statistical analysis was performed with GraphPad Prism 7.0 software. Quantitative results are presented as means \pm standard deviation. Differences among multiple groups were analyzed by one-way ANOVA. The threshold of P value was set at 0.05.

3. Results and discussion

3.1. Preparation and characterization of MPDA@Fe₃O₄-Era

The synthetic route of MPDA@Fe₃O₄-Era was described in Scheme 1. MPDA NPs were obtained by removal of templates after the polymerization process as previously reported [18,19]. Era and Fe₃O₄ were loaded on the surface of MPDA through π - π interaction and/or hydrophobic interaction, respectively. The particle size was less than 250 nm when the ratio of MPDA to erastin was 1:2 (Fig. S1), which was suitable for EPR effect *in vivo*. Meanwhile, the EE % and LC % of MPDA are 79.8% and 24.2%, respectively, when the ratio of MPDA to erastin is 1:2 (Fig. S2). UV-Vis and IR analysis were utilized to confirm the composite of MPDA@Fe₃O₄-Era. A characteristic absorption peak of 295 nm in the UV-Vis spectrum of MPDA@Fe₃O₄-Era indicated the successful loading of Era (Fig. S3). Characteristic absorption peaks of 1670 cm⁻¹ (belong to C=O stretching vibration) and 1100 cm⁻¹ (belong to -O- stretching vibration) in IR spectrum of MPDA@Fe₃O₄-Era confirmed the existence of Era (Fig. S4). In X-ray diffraction (XRD) spectra, the peak positions and relative intensities match well with inverse spinel structure of magnetite (Fig. S5), indicating the successful loading of Fe₃O₄. The loading capability of Era and Fe₃O₄ NPs were calculated to be 25.5% and 10.6%, respectively. MPDA@Fe₃O₄-Era had the spherical morphologies with an approximately diameter of 76 nm, as observed by TEM (Fig. 1a) and SEM (Fig. S6). DLS revealed the average hydrodynamic diameters of MPDA@Fe₃O₄-Era was 196 nm probably due to the highly swelling of MPDA in a hydrated state (Fig. S7). The polydispersity index (PDI) of MPDA@Fe₃O₄-Era was measured to be circa 0.1, indicating their good uniformity. In addition, after storage in water at room temperature for 14 days, MPDA@Fe₃O₄-Era maintained their initial structures and sizes (Fig. S8), exhibited their great dispersibility and stability.



Scheme 1. a) Schematic illustration of the formation of MPDA@Fe₃O₄-Era and (b) the mechanism of synergistic ferroptosis.

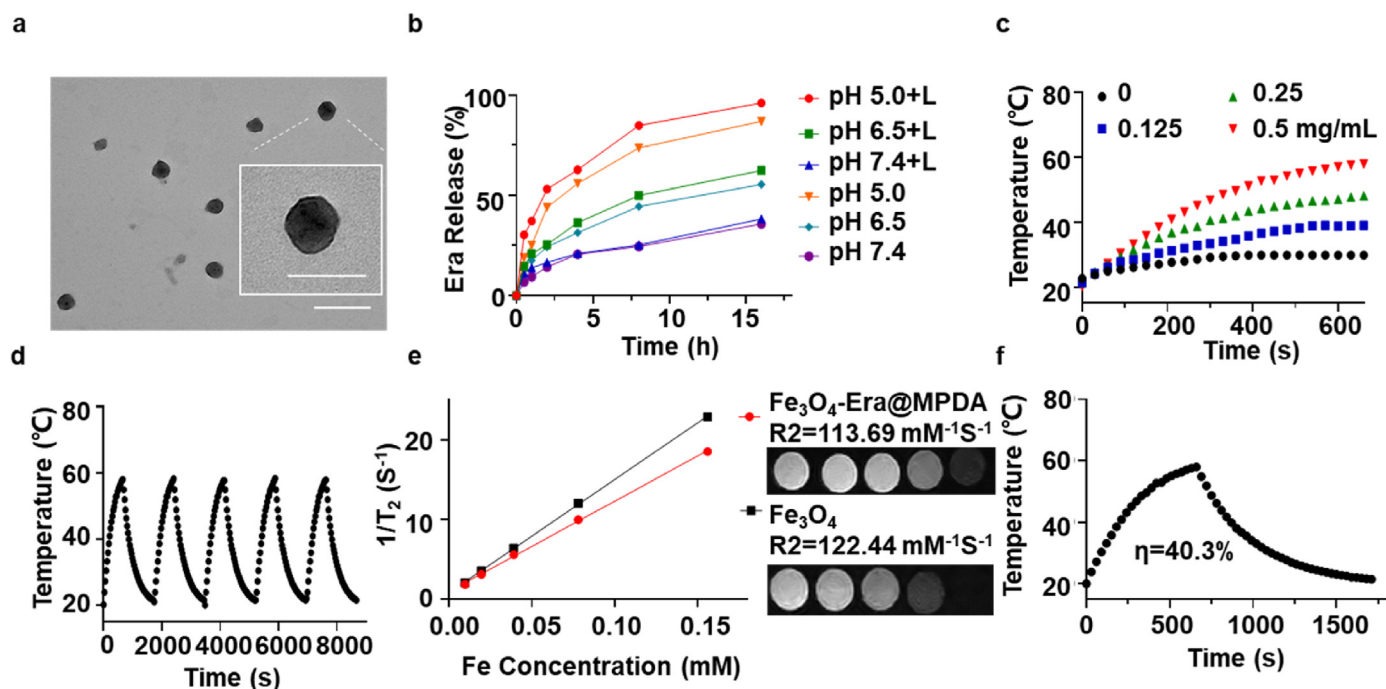


Fig. 1. Characterization of MPDA@Fe₃O₄-Era. (a) TEM of MPDA@Fe₃O₄-Era, the bar was 200 nm and 100 nm (insert image). (b) The cumulative Era release from MPDA@Fe₃O₄-Era at different conditions. (c) Temperature elevations of MPDA@Fe₃O₄-Era solutions at various concentrations with 808 nm laser, 1.5 W cm⁻². (d) Temperature change of MPDA@Fe₃O₄-Era with laser by cooling down for five times. (e) A linear relationship between T₂-weighted MR signal and varying concentrations of Fe. (f) The corresponding linear time data of MPDA@Fe₃O₄-Era under laser. (Laser represents 808 nm laser, and if applied: 1.5 W cm⁻²; n = 3).

Next, we explored the release behaviors of Era and Fe₃O₄ under different pH and NIR stimuli. MPDA@Fe₃O₄-Era showed a sustained Era

and Fe release during 16 h of incubation under pH 7.4 (mimic the physiological environment), 6.5 (mimic the tumor microenvironment)

and 5.0 (mimic the endo/lysosomal microenvironment), respectively (Fig. 1b, Fig. S9). The cumulative Era release were 85.4%, 56.1% and 34.7% at 16 h under pH 5.0, pH 6.5 and pH 7.4, respectively. Besides, 47.5% of Fe ions were released from MPDA@Fe₃O₄-Era within 16 h under pH 6.5, and 73.7% of Fe ions were released under pH 5.0. In contrast, only 21.7% of Fe ions were released in pH 7.4 solution within 16 h. The cumulative Era and Fe ions release increased to 96.5% and 88.6% at 16 h with laser (1.5 W cm⁻², 6 min) under pH 5.0 condition, respectively (Fig. 1b, Fig. S9). The results indicated the release of Era and Fe ions was expedited by acidic and NIR laser stimuli.

The PTT performance of MPDA@Fe₃O₄-Era solution was evaluated subsequently. As shown in Fig. 1c, solution temperature increased to ~58.0 °C at a concentration of 0.25 mg mL⁻¹ MPDA@Fe₃O₄-Era that received 1.5 W cm⁻² NIR irradiation for 10 min. When the power density raised to 2 W cm⁻², the solution temperature increased to ~70.6 °C (Fig. S10). To investigate the photothermal stability, the MPDA@Fe₃O₄-Era aqueous solution was placed under periodically irradiation of 808 nm laser. After five “ON/OFF” cycles, the maximum temperatures of MPDA@Fe₃O₄-Era solution maintained unchanged, demonstrating the outstanding photostability (Fig. 1d). The photothermal conversion efficiency (η) of MPDA@Fe₃O₄-Era was calculated to be 40.3% (Fig. 1f, Fig. S11), which is superior than the majority of photothermal agents, including Au nanorod (27.1%) [20], MPDA (38.7%) [19] and CuS NPs (27.2%) [21]. Thus, MPDA@Fe₃O₄-Era could be a promising candidate for PTT applications in cancer therapy for the remarkable photothermal conversion capability and excellent photostability.

To explore the MRI capability of MPDA@Fe₃O₄-Era, the transverse relaxivity (R₂) of a MPDA@Fe₃O₄-Era and Fe₃O₄ aqueous solution were measured by MRI scanner. As shown in Fig. 1e, T₂-weighted images of

MPDA@Fe₃O₄-Era remarkably enhanced with increasing concentrations of MPDA@Fe₃O₄-Era. The R₂ values of MPDA@Fe₃O₄-Era was measured to be 113.69 mM⁻¹s⁻¹, which is slightly lower than 122.44 mM⁻¹s⁻¹ of Fe₃O₄. The results indicated that MPDA@Fe₃O₄-Era had T₂-weighted MRI intensity for tumor diagnosis.

3.2. In vitro ferrotherapy

Higher uptake rates of drugs induced higher rates of tumor cell death [22]. Rh B labeled MPDA@Fe₃O₄-Era was employed to investigate cellular uptake. By using CLSM, we found that the red fluorescence of Rh B/MPDA@Fe₃O₄-Era co-localized with blue fluorescence signal of DAPI in a time-dependent manner (Fig. 2a). Quantitatively FCM analysis revealed the endocytosis of MPDA@Fe₃O₄-Era increased within 2 h incubation time (Fig. 2b, Fig. S12), suggesting NIR laser should be used after 2 h.

The cytotoxicity of MPDA@Fe₃O₄-Era toward 4T1 cells was first determined by CCK8 assay. There is a concentration- and power intensity-dependent 4T1 cytotoxicity after treated with MPDA@Fe₃O₄-Era (Fig. S13 and S14). Significantly, among all the groups with different laser power and concentrations, almost all 4T1 cells died when these cells were irradiated by 808 nm laser (1.5 W cm⁻²) at a concentration of 100 μ g mL⁻¹ MPDA, which applied for following experiments. Next, to determine the contribution of each component in killing cancer cells in MPDA@Fe₃O₄-Era, the treatments were divided into 6 groups as follows: Control, MPDA, MPDA@Fe₃O₄, MPDA@Era, MPDA@Fe₃O₄-Era, MPDA@Fe₃O₄-Era plus laser (808 nm, 1.5 W cm⁻², 6 min). MPDA@Fe₃O₄-Era plus laser group and MPDA@Fe₃O₄-Era group showed 42.3% and 64.6% cell viabilities, respectively, while MPDA group exhibited

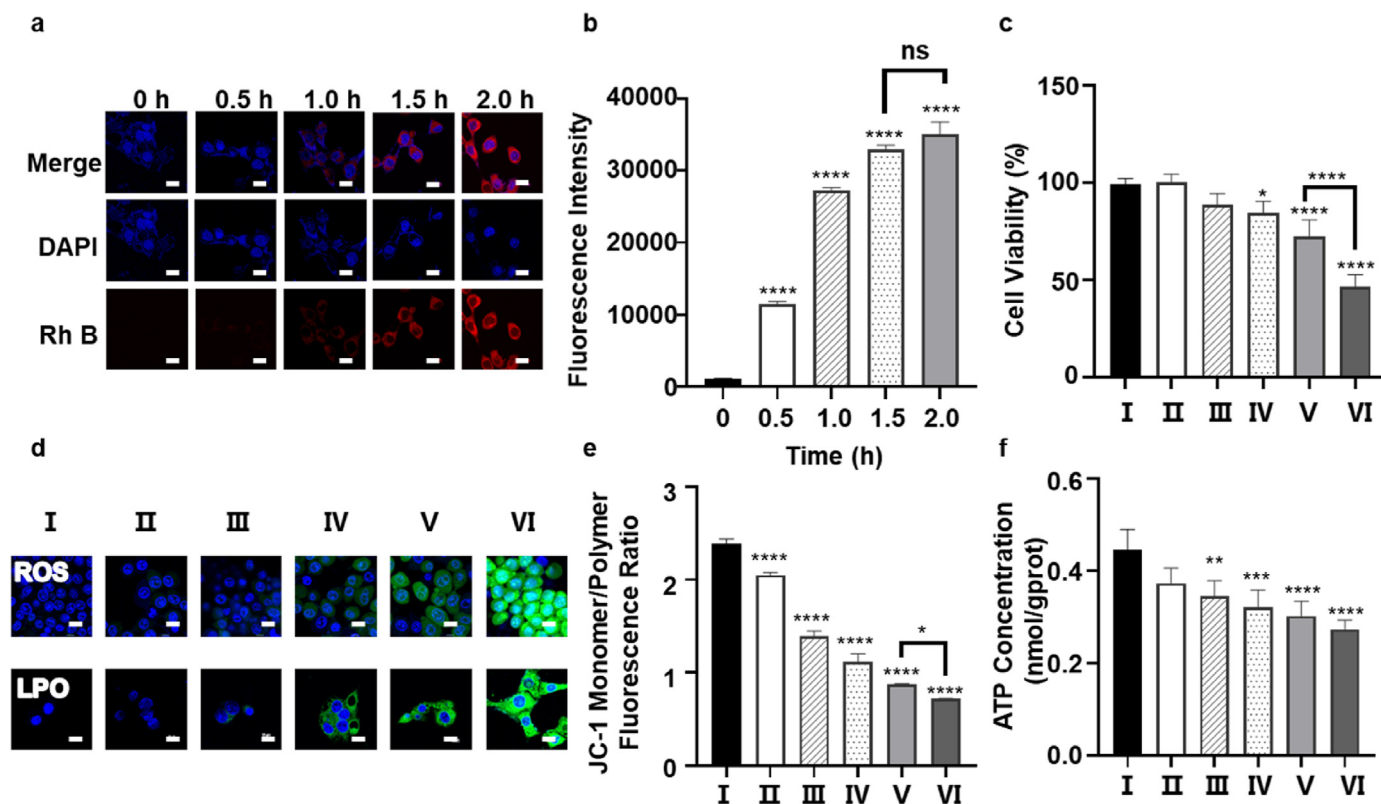


Fig. 2. Cell uptake and cytotoxicity *in vitro*. 4T1 cells incubated with MPDA@Fe₃O₄-Era at different time. (a) CLSM; bar was 10 μ m. (b) FCM. (c) Cell viabilities of 4T1 cells after the co-incubation with different formulations. (d) CLSM images of 4T1 cells stained by DCFH-DA (ROS probe) and C11BODIPY (LPO probes) after treated with different formulations for 6 h; the bar was 10 μ m. (e) Quantitative fluorescence intensity of 4T1 cells stained by JC-1 probe in different formulations for 6 h by FCM. (f) ATP levels of 4T1 cells after treated with different formulations for 6 h (I) Control, (II) MPDA, (III) MPDA@Fe₃O₄, (IV) MPDA@Era, (V) MPDA@Fe₃O₄-Era and (VI) MPDA@Fe₃O₄-Era plus laser. Laser represents 808 nm laser, and if applied: 1.5 W cm⁻², 6 min; concentration if applied: 100 μ g mL⁻¹ MPDA; n = 3; *, **, *** and **** indicate P < 0.05, P < 0.01, P < 0.001 and P < 0.0001 respectively.).

negligible cell death at the same concentration (cell viabilities >90%) (Fig. 2c). These results indicated laser irradiation significantly enhanced MPDA@Fe₃O₄-Era induced 4T1 cells cytotoxicity and there is a synergistic effect between phototherapy and chemotherapy. The similar cytotoxicity pattern was achieved by a live/dead cell staining analysis (Fig. S15).

Abundant generation of ROS in the cell could cause oxidative damage to lipids, proteins and DNA, further lead to cell death [23]. Intracellular ROS was detected using DCFH-DA as a fluorescent probe. It was obviously found that MPDA@Fe₃O₄-Era plus laser group showed strongest green fluorescence in comparison with other groups (Fig. 2d, Fig. S16), suggesting large ROS generation. Subsequently, electron spin-resonance (ESR) spectroscopy analysis was conducted to detect the formed ROS species. Characteristic ESR signal of DMPO/•OH (1:2:2:1) appeared with the addition of MPDA@Fe₃O₄-Era and Fe₃O₄ NPs (Fig. S17). Next, C11BOD-IPY was selected as a fluorescent indicator to evaluate LPO levels by monitoring their fluorescence intensity (Fig. 2d, Fig. S18). The above results indicated that MPDA@Fe₃O₄-Era under laser irradiation produce abundant ROS and LPO ending products.

Endogenous ROS accumulated in the mitochondria, then triggered DNA damage intracellularly [24]. Therefore, JC-1 staining was employed to evaluate the mitochondria dysfunction. JC-1 mainly existed as aggregates without obvious mitochondrial depolarization in control and MPDA groups (Fig. 2e). The decrease of red spots and the increase of green spots were observed in MPDA@Fe₃O₄-Era plus laser groups compared with other groups, indicating the mitochondrial depolarization after these treatments (Fig. S19). These results demonstrated that MPDA@Fe₃O₄-Era regulated the level of endogenous ROS to disrupt mitochondrial function, resulting in 4T1 cell death. Besides, the decrease of ROS generation in the proton gradient across the inner mitochondrial membrane is the driving force of ATP production [25]. The intracellular ATP levels of MPDA@Fe₃O₄-Era plus laser group significantly reduced compared with other groups, indicating significantly mitochondrial damage owing to ROS generation (Fig. 2f).

3.3. *In vitro* ferrotherapy mechanism

The regulatory mechanisms of ferroptosis are summarized to ROS (particularly LPO) mechanism, iron metabolism and amino acid and glutathione metabolism [26]. In this study, MPDA@Fe₃O₄-Era showed advantages on these aspects. As demonstrated in Fig. 3a, system X_C⁻ mediates the exchange of extracellular Cys and intracellular Glu through the cell membrane [27]. Inhibition of system X_C⁻-mediated Cys import would lead to the depletion of intracellular GSH, inactive of GPX4 and further induce ferroptosis [28]. Meanwhile, iron regulated by TFR, FPN1 and FTH1 protein expressions triggers the Fenton reaction and generates LPO ending products, which further promotes the occurrence of ferroptosis [29]. Thus, the compromise of HSPs protein function is beneficial for PTT efficiency.

Specific promoter (Glu, inhibit Cys import to cell) and inhibitor (Cys, synthesize GSH to inhibit ferroptosis) were applied to test the influence of system X_C⁻ signal pathway of ferroptosis in MPDA@Fe₃O₄-Era-treated 4T1 cells. As shown in Fig. S20, Glu obviously enhanced the cytotoxicity of MPDA@Fe₃O₄-Era, while Cys alleviated 13.7% cell death. MDA assay showed that MPDA@Fe₃O₄-Era treatment caused a rapid generation of MDA, the final-product of LPO from ferroptosis (Fig. 3b). Meanwhile, GSH level significantly decreased following MPDA@Fe₃O₄-Era treatment compared with the control (Fig. 3c). MPDA@Fe₃O₄-Era-induced reduction in GSH level and increase in MDA content were all blocked by simultaneous treatment with Glu, which was opposite with the co-treatment with Cys. GPX4, ACSL4 (an essentially pro-ferroptotic gene) and SLC7A11 (a functional subunit of system X_C⁻) protein expressions were investigated by Western blotting analysis (Fig. 3d). Obvious downregulation of GPX4 and SLC7A11 protein levels were found in MPDA@Fe₃O₄-Era treated groups, which was opposite with the expression of ACSL4. These results showed MPDA@Fe₃O₄-Era could induce

ferroptosis through mediating system X_C⁻ signal pathway. In the MPDA@Fe₃O₄-Era plus Cys group, the expressions of SLC7A11 and GPX4 protein were upregulated and ACSL4 was downregulated. Collectively, these findings suggested that MPDA@Fe₃O₄-Era decrease GSH biosynthesis, regulate GPX4, SLC7A11, ACSL4 protein expressions and enhance MDA biosynthesis to promote ferroptosis in 4T1 cells.

Subsequently, we explored the effect of iron metabolism on the contribution of MPDA@Fe₃O₄-Era-induced cytotoxicity by using a specific inhibitor DFP (iron chelator). Obviously, DFP increased 53.6% cell viabilities compared with MPDA@Fe₃O₄-Era (Fig. S21). In addition, the results showed cytosolic labile iron levels significantly increased in MPDA@Fe₃O₄-Era-treated 4T1 cells, whereas remarkably alleviated excessive cytosolic iron concentration after administration of DFP. The results implied that MPDA@Fe₃O₄-Era could increase cytosolic labile iron levels and further lead to cell death (Fig. S22). TFR, FPN1 and FTH1 proteins, as the key proteins mediated iron concentration, were investigated by Western blotting analysis. As shown in Fig. 3e, MPDA@Fe₃O₄-Era increased the levels of TFR proteins, but inhibited FTH1 and FPN1 expressions in 4T1 cells; administration with DFP significantly increased the levels of FTH1 and FPN1 and inhibited the levels of TFR protein compared with MPDA@Fe₃O₄-Era group, implying MPDA@Fe₃O₄-Era accelerated the intracellular iron overloaded in an attempt to promote iron metabolism. Consistent real-time quantitative PCR (RT-qPCR) analysis was achieved (Fig. S23). In conclusion, these results implied MPDA@Fe₃O₄-Era trigger ferroptosis through co-regulating the signal pathway of system X_C⁻ and iron metabolism, which generated excess ROS and LPO ending products and augment ferroptosis therapy.

As we hypothesized ROS and LPO ending products cross-linked HSP protein, the synergistic mechanism of photothermal ferrotherapy was investigated. As shown in Fig. S24, MPDA@Fe₃O₄-Era plus laser treatment has 31.2% cell viabilities, while 60.2% for MPDA plus laser treatment and 46.8% for MPDA@Era plus laser treatment, suggesting the synergistic ferro-photothermal therapy. Western blot assay was carried out to evaluate the HSP70 (one main variety of HSPs) expression levels in 4T1 cells after different treatments. Obviously, the level of HSP70 protein decreased in MPDA@Fe₃O₄ plus laser and MPDA@Era plus laser treatment group, compared with MPDA NPs plus laser, indicating that ferroptosis inducer decrease HSP70 protein expression. Furthermore, the level of HSP70 protein of MPDA@Fe₃O₄-Era plus laser group was lowest among all the groups with laser irradiation, suggesting dual-ferrotherapy furtherly decrease HSP70 protein expression (Fig. S25). Cell viability assay showed that MPDA NPs plus VER155008 (an inhibitor of HSP70) and laser treatment decreased compared with MPDA NPs plus laser treatment (Fig. 3f). It was found that the supplementation of Eugenol (the inhibitor of LPO) and Fer-1 (the inhibitor of ferroptosis) increased cell viability compared with MPDA@Fe₃O₄-Era, indicating cell death influenced by LPO. The above results indicated HSPs protein and LPO played important role in cell death. HSP70 protein expression increased under laser irradiation, which could be reversed by VER155008 (Fig. 3g, Fig. S26). Eugenol and Fer-1 treatment increased HSP70 protein expression in MPDA@Fe₃O₄-Era plus laser group, also suggested the LPO ending products on the inhibition of HSP70 protein. All the results demonstrated HSP70 would be downregulated by LPO ending products from ferroptosis inducer.

3.4. *In vivo* fluorescence, MRI and thermal imaging

Biodistribution of MPDA@Fe₃O₄-Era was investigated in a 4T1 tumor-bearing mouse model. For *in vivo* monitoring, Cy5 labeled MPDA@Fe₃O₄-Era were fabricated to track the distribution of MPDA@Fe₃O₄-Era in mice [30]. After intravenously injected with Cy5-labeled MPDA@Fe₃O₄-Era, the fluorescence signals increased within 12 h and then decayed at 24 h, ascribe to the EPR effect of NPs (Fig. 4a). A large proportion of NPs were entrapped in the liver and kidneys of the mice, which could be attributed to the uptake of the reticuloendothelial system (Fig. 4b).

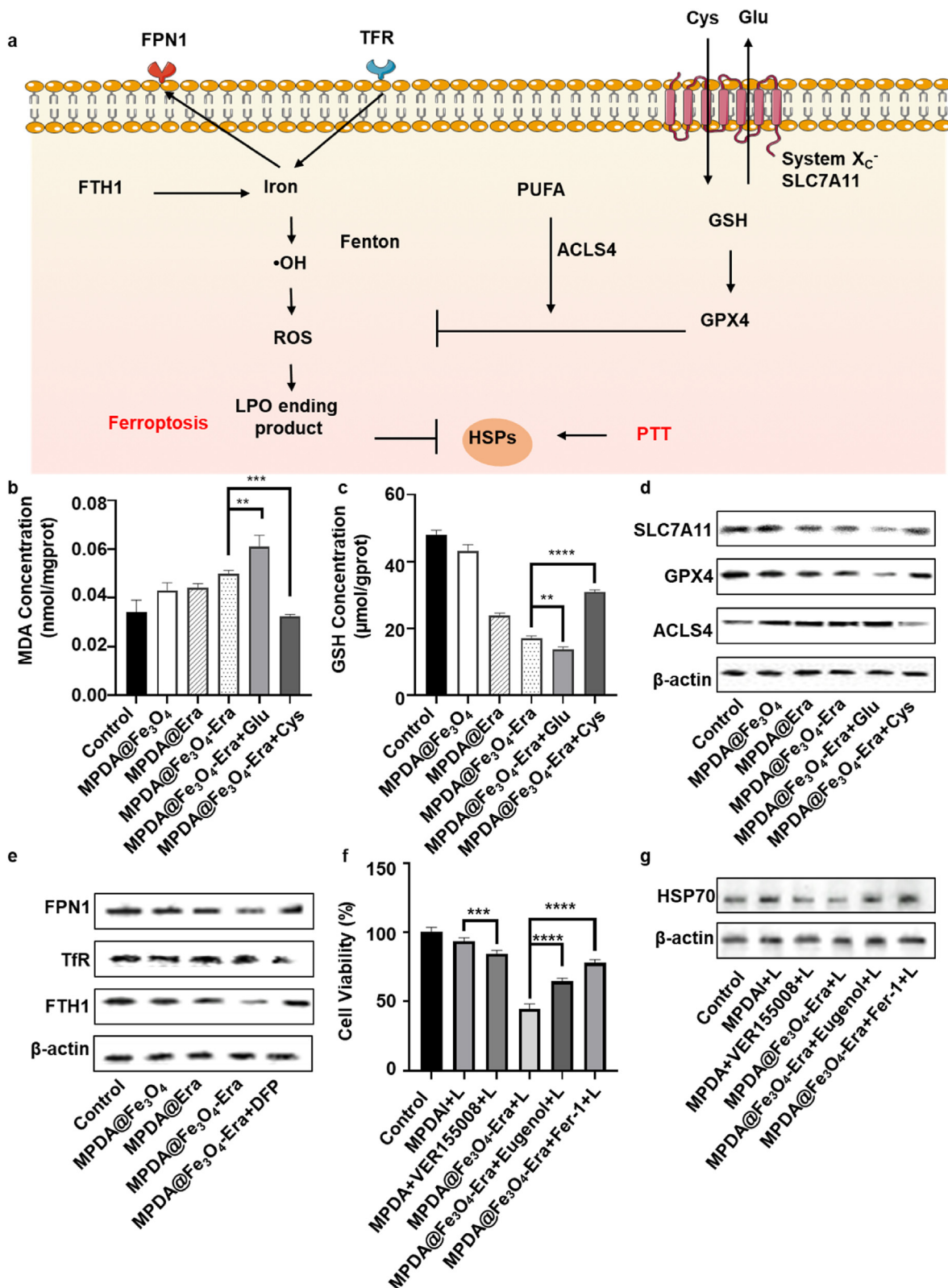


Fig. 3. Mechanism of MPDA@Fe₃O₄-Era induced dual-ferroptosis therapy. (a) Schematic diagram of synergistic ferroptosis. (b) MDA level of 4T1 cells after treated with Glu (2 mM), Cys (2 mM) in MPDA@Fe₃O₄-Era for 24 h. (c) GSH level of 4T1 cells after treated with Glu (2 mM), Cys (2 mM) in MPDA@Fe₃O₄-Era for 24 h. (d) Western blot analysis of GPX4, SLC7A11 and ACSL4 expressions in 4T1 cells after the treatment with different formulations. (e) Western blot analysis of FPN1, TfR and FTH1 expressions in 4T1 cells after the treatment with different formulations. (f) Cell viability in 4T1 cells after the treatment with different formulations. (g) Western blot analysis of HSP70 expression in 4T1 cells after the treatment with different formulations. (Laser represents 808 nm laser, and if applied: 1.5 W cm⁻², 6 min; concentration if applied: 100 μg mL⁻¹ MPDA; n = 3; **, *** and **** indicate P < 0.01, P < 0.001 and P < 0.0001 respectively).

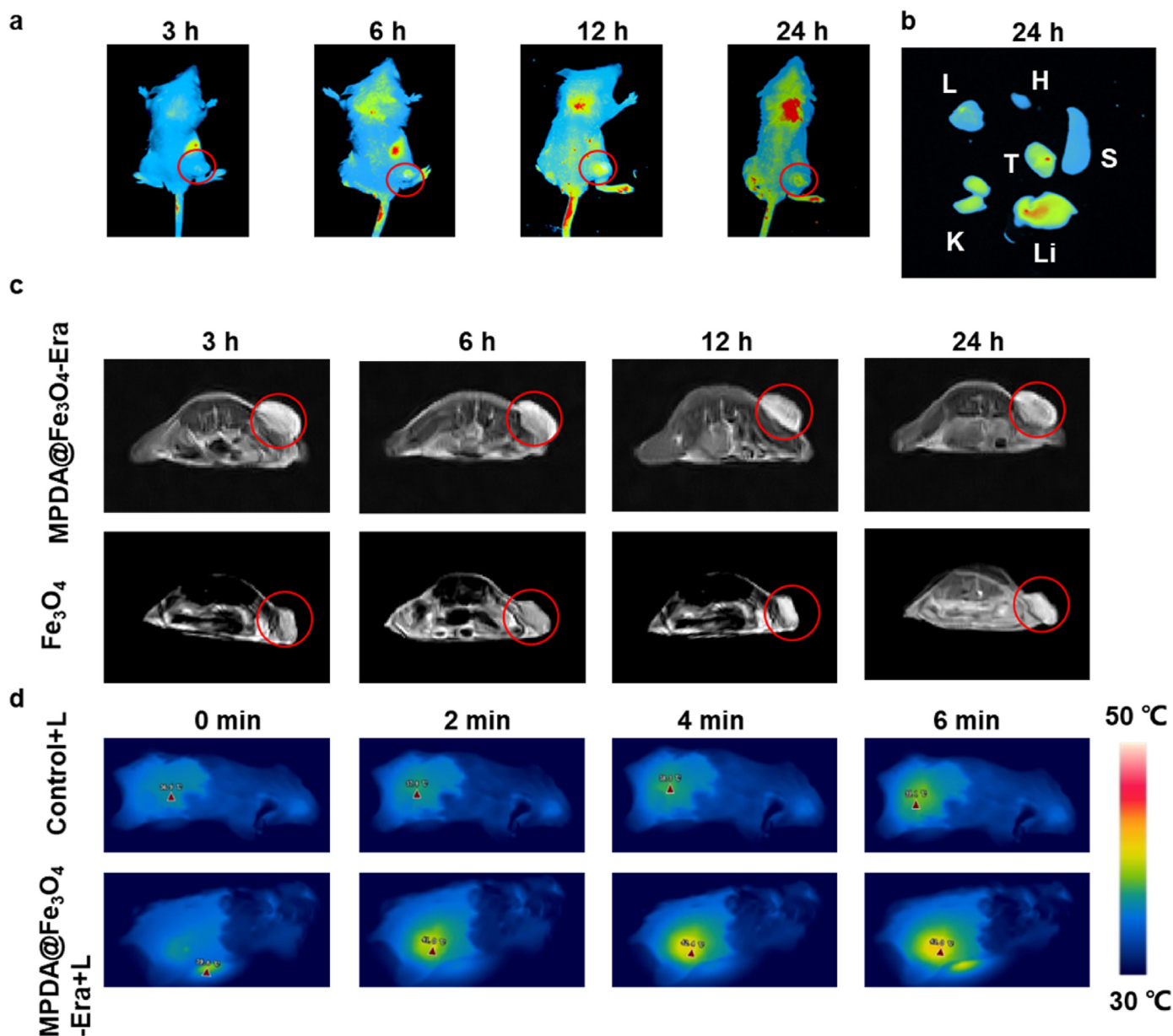


Fig. 4. *In vivo* imaging of MPDA@Fe₃O₄-Era. (a) *In vivo* fluorescence images of 4T1 tumor-bearing mice at different time points after intravenous injection of Cy5-labeled MPDA@Fe₃O₄-Era. (b) *Ex vivo* fluorescence image of major organs and tumors at 24 h after intravenous injection of Cy5-labeled MPDA@Fe₃O₄-Era. (c) *In vivo* T2-weighted MR images of 4T1 tumor-bearing mice at different time points after intravenous injection of MPDA@Fe₃O₄-Era and Fe₃O₄. (d) Thermal images of 4T1 tumor-bearing mice under laser irradiation at different time points after intravenous injection of MPDA@Fe₃O₄-Era. (L represents lung, Liv represents liver, T represents tumor, K represents kidney, H represents heart, S represents spleen; Laser represents 808 nm laser, and if applied: 1.5 W cm⁻², 6 min; Dose if applied: 15 mg kg⁻¹ MPDA; n = 3).

We next evaluated the tumor-targeting performance of MPDA@Fe₃O₄-Era and Fe₃O₄ NPs *in vivo* by MRI. After injection, the T2-weight imaging signal intensity of Fe₃O₄ NPs in tumor areas remained until 6 h due to rapid metabolism of small particles *in vivo*. While the T2-weighted imaging signal intensity of MPDA@Fe₃O₄-Era in the tumor area remained excellent T2 contrast effect until 12 h compared with a group of Fe₃O₄ NPs (Fig. 4c).

The potential of MPDA@Fe₃O₄-Era for photothermal therapy *in vivo* was examined by an infrared camera, which was used to record the tumor temperature changes every minute during the NIR irradiation. The tumor temperature in group of MPDA@Fe₃O₄-Era plus laser rapidly increased to 42.3 °C within 6 min, whereas that of the PBS group only reached 39.1 °C, suggesting that MPDA@Fe₃O₄-Era effectively produce proper temperature to achieve mild-temperature PTT treatment (Fig. 4d). The

temperature cumulative curve was consistent with the results of infrared camera (Fig. S27), suggesting the successful mild-temperature PTT *in vivo*. Based on imaging results, the optimal NIR laser irradiation was applied under the 808 nm laser with a power of 1.5 W cm⁻² after 12 h post-intravenous injection of MPDA@Fe₃O₄-Era.

3.5. *In vivo* ferrotherapy and biosafety evaluation

We further explored the ferrotherapy activity of MPDA@Fe₃O₄-Era using 4T1 tumor-bearing mice. Mice were intravenously injected with different formulations on day 2, 5 and 8 at 15 mg kg⁻¹ MPDA, while laser applied 12 h after intravenously injection (Fig. 5a). When the tumor sizes reached 80–100 mm³, the mice were randomly divided into six groups (n = 5): (I) PBS, (II) MPDA, (III) MPDA@Fe₃O₄, (IV) MPDA@Era, (V)

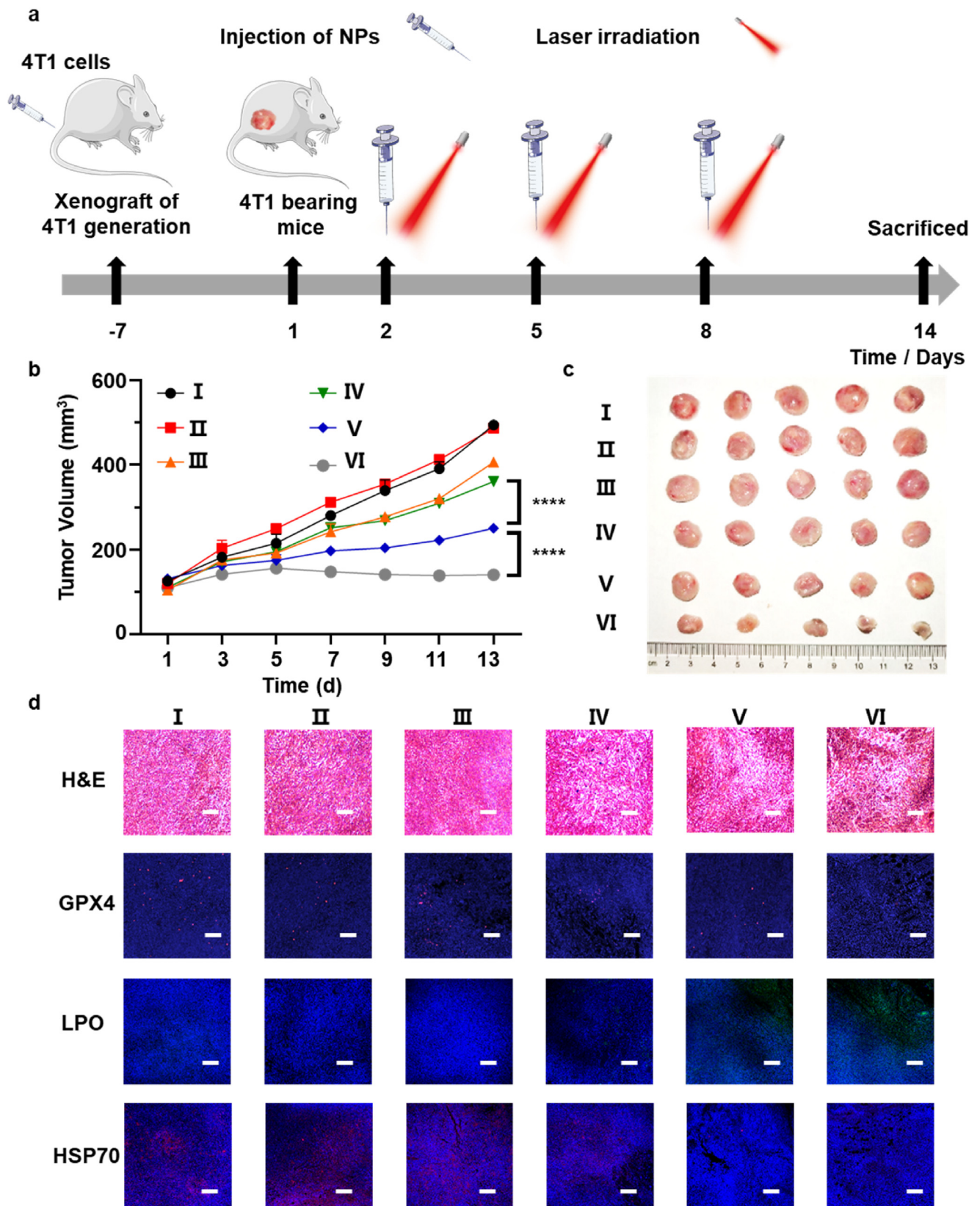


Fig. 5. *In vivo* antitumor performance evaluation of MPDA@Fe₃O₄-Era. (a) Timeline of different treatment. 4T1 tumor-bearing mice were treated with injections of different groups on the 2nd, 5th and 8th days. (b) Variation of tumor volume during 14 days of treatments (n = 5). (c) Photographs of tumors obtained at the 14th day after treatments (n = 5). (d) Histological observation of the tumors with H&E staining, GPX4, LPO and HSP70 staining from 14 days of different treatments; the bar was 100 μ m. (I) Control, (II) MPDA, (III) MPDA@Fe₃O₄, (IV) MPDA@Era, (V) MPDA@Fe₃O₄-Era and (VI) MPDA@Fe₃O₄-Era plus laser. Laser represents 808 nm laser, and if applied: 1.5 W cm⁻², 6 min; Laser irradiation was applied to tumor at 12 h post-injection; Dose if applied: 15 mg kg⁻¹ MPDA; **** indicate P < 0.0001).

MPDA@Fe₃O₄-Era and (VI) MPDA@Fe₃O₄-Era plus laser. The tumor volumes of the mice in each group were recorded every two days. As shown in Fig. 5b, MPDA treatment did not inhibit tumor growth compared with PBS group. On the contrary, MPDA@Fe₃O₄-Era treatment suppressed the volume and size of tumor, attributed to the promising antitumor effect of ferroptosis therapy. The tumor growth was efficiently suppressed by MPDA@Fe₃O₄-Era plus laser treatment group showed the most efficient on the inhibition of tumor group. After 13 days, the dissected tumors from all groups were photographed and weighted (Fig. 5c, Fig. S28). The tumor size and weight of the MPDA@Fe₃O₄-Era plus laser irradiation group were less than all the other groups, revealing the dual-ferro-photothermal therapy *in vivo*. Next, H&E staining was performed to estimate the anti-cancer therapeutic effects. Compared to other groups, nuclear dissociation and tissue necrosis of tumor were evident in MPDA@Fe₃O₄-Era plus laser irradiation group (Fig. 5d), suggesting the strongest antitumor effect of dual-ferro-photothermal therapy group. In addition, immunofluorescence analysis of GPX4 found that MPDA@Fe₃O₄-Era simultaneously decreased GPX4 protein expression compared with the control group, while the MPDA@Fe₃O₄-Era plus laser treatment showed the least GPX4 protein expression (Fig. 5d), indicating the occurrence of ferroptosis and PTT. There is low LPO expression in control and MPDA group, suggesting no occurrence of ferroptosis. The LPO expression increased in MPDA@Fe₃O₄, MPDA@Era and MPDA@Fe₃O₄-Era treatments, indicating the exist of ferroptosis. There was highest LPO levels in MPDA@Fe₃O₄-Era plus laser treatment, indicating combination of ferroptosis and PTT. We also found that decreased HSP70 protein expression of MPDA@Fe₃O₄-Era plus laser treatment compared with other groups, indicating synergistic hydroxyl radical formation, system X_C⁻ inhibition and heat shock protein cross-linking tango in ferrotherapy (Fig. 5d).

Evaluating systemic toxicity is critical for nanomaterials clinical research. The body weights of mice in all groups kept stable during the therapeutic period (13 days), indicating that all the treatments had low toxicity and negligible side effect on the mice (Fig. S29). Major organs (heart, liver, spleen, lung, and kidneys) of mice were collected at post-13 days treatments to evaluate the NPs safety. H&E stained sections of major organs showed that no significant organ damages were caused by all the groups (Fig. S30). Moreover, various blood biochemical parameters (albumin, ALB; alanine aminotransferase, ALT; urea nitrogen, BUN) were all within the normal reference ranges as compared with the control group, which indicated that different treatments induced no obvious toxicity of the liver and kidneys within 13 days (Fig. S31). The biological safety was further investigated *via* analysis of biochemical indexes, including white blood cell (WBC) count, red blood cell (RBC) count, lymphocyte (Lymph) percentage, monocytes (Mon) percentage, gran (Gran) percentage, hematocrit (HCT), red cell distribution width (RDW), platelet hematocrit (PCT), platelet (PLT) count. Compared with the control group, these markers were still in the normal range with different treatments (Fig. S32). These results demonstrated that MPDA@Fe₃O₄-Era possessed good biological safety.

4. Conclusion

A smart theranostic MPDA@Fe₃O₄-Era was constructed to achieve MRI-guided dual-ferroptosis therapy. MPDA@Fe₃O₄-Era were responsive to pH and NIR stimuli to release Fe₃O₄ and Era and induced cancer cell death. Mechanistically, MPDA@Fe₃O₄-Era could release Fe₃O₄ to enhance the intracellular concentration of iron under tumor acid microenvironment and laser irradiation. Meanwhile, MPDA@Fe₃O₄-Era could inhibit system X_C⁻ to suppress the exchange of Cys and Glu, which depleted GSH *via* GPX4-inactivating signal pathway. ROS and LPO ending products crosslink HSPs to destroy the self-preservation of cancer cell enhance the efficacy of ferroptosis therapy. Hence, the proposed dual-ferrotherapy strategy possesses the outstanding theranostic effect for anti-tumor therapy and deserved further explorations towards applications of ferroptosis in anticancer fields.

Credit author statement

L. X., X. Z. and Y. S. designed research; L. X., W. C., Q. C. and Y. J. performed research; E. S. and Y. S. contributed reagents/analytic tools; L. X., W. C., Q. C., Y. J., X. Z. and Y. S. analyzed data; L. X., X. Z. and Y. S. wrote the paper.

Declaration of competing interest

The authors declare that they have no known competing financial interests or personal relationships that could have appeared to influence the work reported in this paper.

Acknowledgements

This work is financially supported by Fundamental Research Funds for the Central Universities (XDJK 2020C062), Natural Science Foundation of Chongqing, China (cstc2021jcyj-msxmX1026) and National Natural Science Foundation of China (21976145 and 22176206).

Appendix A. Supplementary data

Supplementary data to this article can be found online at <https://doi.org/10.1016/j.mtbio.2022.100353>.

References

- [1] K. Pierzynowska, E. Rintz, L. Gaffke, G. Wegrzyn, Ferroptosis and its modulation by autophagy in light of the pathogenesis of lysosomal storage diseases, *Cells* 10 (2) (2021).
- [2] L. Jiang, N. Kon, T. Li, S.J. Wang, T. Su, H. Hibshoosh, R. Baer, W. Gu, Ferroptosis as a p53-mediated activity during tumour suppression, *Nature* 520 (7545) (2015) 57–62.
- [3] Z. Tang, Z. Huang, Y. Huang, Y. Chen, M. Huang, H. Liu, Q.A. Ye, J. Zhao, B. Jia, Ferroptosis: the silver lining of cancer therapy, *Front. Cell Dev. Biol.* 9 (2021), 765859.
- [4] S. Wang, F. Li, R. Qiao, X. Hu, H. Liao, L. Chen, J. Wu, H. Wu, M. Zhao, J. Liu, R. Chen, X. Ma, D. Kim, J. Sun, T.P. Davis, C. Chen, J. Tian, T. Hyeon, D. Ling, Arginine-rich manganese silicate nanobubbles as a ferroptosis-inducing agent for tumor-targeted theranostics, *ACS Nano* 12 (12) (2018) 12380–12392.
- [5] Z. Shi, N. Naowarajna, Z. Pan, Y. Zou, Multifaceted mechanisms mediating cystine starvation-induced ferroptosis, *Nat. Commun.* 12 (1) (2021) 4792.
- [6] W.S. Yang, R. SriRamaratnam, M.E. Welsch, K. Shimada, R. Skouta, V.S. Viswanathan, J.H. Cheah, P.A. Clemons, A.F. Shamji, C.B. Clish, L.M. Brown, A.W. Girotti, V.W. Cornish, S.L. Schreiber, B.R. Stockwell, Regulation of ferroptotic cancer cell death by GPX4, *Cell* 156 (1–2) (2014) 317–331.
- [7] W.S. Yang, K.J. Kim, M.M. Gaschler, M. Patel, M.S. Shchepinov, B.R. Stockwell, Peroxidation of polyunsaturated fatty acids by lipoxygenases drives ferroptosis, *Proc. Natl. Acad. Sci. U. S. A.* 113 (34) (2016) E4966–E4975.
- [8] S. Zhu, Q. Zhang, X. Sun, H.J. Zeh 3rd, M.T. Lotze, R. Kang, D. Tang, HSPA5 regulates ferroptotic cell death in cancer cells, *Cancer Res.* 77 (8) (2017) 2064–2077.
- [9] X. Sun, Z. Ou, M. Xie, R. Kang, Y. Fan, X. Niu, H. Wang, L. Cao, D. Tang, HSPB1 as a novel regulator of ferroptotic cancer cell death, *Oncogene* 34 (45) (2015) 5617–5625.
- [10] X. Jiang, B.R. Stockwell, M. Conrad, Ferroptosis: mechanisms, biology and role in disease, *Nature reviews, Mol. Cell Biol.* 22 (4) (2021) 266–282.
- [11] W. Hou, Y. Xie, X. Song, X. Sun, M.T. Lotze, H.J. Zeh 3rd, R. Kang, D. Tang, Autophagy promotes ferroptosis by degradation of ferritin, *Autophagy* 12 (8) (2016) 1425–1428.
- [12] M. Gao, P. Monian, N. Quadri, R. Ramasamy, X. Jiang, Glutaminolysis and transferrin regulate ferroptosis, *Mol. Cell* 59 (2) (2015) 298–308.
- [13] J.E. Hudak, H.H. Yu, C.R. Bertozzi, Protein glycoengineering enabled by the versatile synthesis of aminoxy glycans and the genetically encoded aldehyde tag, *J. Am. Chem. Soc.* 133 (40) (2011) 16127–16135.
- [14] F. Zeng, L. Tang, Q. Zhang, C. Shi, Z. Huang, S. Nijjati, X. Chen, Z. Zhou, Coordinating the mechanism of actions of ferroptosis and photothermal effect for cancer theranostics, *Angew. Chem. Int. Ed. Engl.* 61 (2022), e202112925.
- [15] Y. Liu, Q. Fan, Y. Huo, C. Liu, B. Li, Y. Li, Construction of a mesoporous polydopamine@GO/cellulose nanofibril composite hydrogel with an encapsulation structure for controllable drug release and toxicity shielding, *ACS Appl. Mater. Interfaces* 12 (51) (2020) 57410–57420.
- [16] G. Shu, M. Chen, J. Song, X. Xu, C. Lu, Y. Du, M. Xu, Z. Zhao, M. Zhu, K. Fan, X. Fan, S. Fang, B. Tang, Y. Dai, Y. Du, J. Ji, Sialic acid-engineered mesoporous polydopamine nanoparticles loaded with SPIO and Fe(3+) as a novel theranostic agent for T1/T2 dual-mode MRI-guided combined chemo-photothermal treatment of hepatic cancer, *Bioact. Mater.* 6 (5) (2021) 1423–1435.

- [17] Y. Zhu, N. Xin, Z. Qiao, S. Chen, L. Zeng, Y. Zhang, D. Wei, J. Sun, H. Fan, Novel tumor-microenvironment-based sequential catalytic therapy by Fe(II)-Engineered polydopamine nanoparticles, *ACS Appl. Mater. Interfaces* 11 (46) (2019) 43018–43030.
- [18] Y. Liu, Q. Fan, Y. Huo, C. Liu, B. Li, Y. Li, Construction of a mesoporous polydopamine@GO/cellulose nanofibril composite hydrogel with an encapsulation structure for controllable drug release and toxicity shielding, *ACS Appl. Mater. Interfaces* 12 (51) (2020) 57410–57420.
- [19] L. Wang, Y. He, T. He, G. Liu, C. Lin, K. Li, L. Lu, K. Cai, Lymph node-targeted immune-activation mediated by imiquimod-loaded mesoporous polydopamine based-nanocarriers, *Biomaterials* 255 (2020), 120208.
- [20] S. Wang, J. Lin, Z. Wang, Z. Zhou, R. Bai, N. Lu, Y. Liu, X. Fu, O. Jacobson, W. Fan, J. Qu, S. Chen, T. Wang, P. Huang, X. Chen, Core-satellite polydopamine-gadolinium-metallofullerene nanotheranostics for multimodal imaging guided combination cancer therapy, *Adv. Mater.* 29 (35) (2017), 1701013.
- [21] D. Jana, S. Jia, A.K. Bindra, P. Xing, D. Ding, Y. Zhao, Clearable black phosphorus nanoconjugate for targeted cancer phototheranostics, *ACS Appl. Mater. Interfaces* 12 (16) (2020) 18342–18351.
- [22] J. Pascal, C.E. Ashley, Z. Wang, T.A. Brocato, J.D. Butner, E.C. Carnes, E.J. Koay, C.J. Brinker, V. Cristini, Mechanistic modeling identifies drug-uptake history as predictor of tumor drug resistance and nano-carrier-mediated response, *ACS Nano* 7 (12) (2013) 11174–11182.
- [23] B. Wang, H. Zhang, J. An, Y. Zhang, L. Sun, Y. Jin, J. Shi, M. Li, H. Zhang, Z. Zhang, Sequential intercellular delivery nanosystem for enhancing ROS-induced antitumor therapy, *Nano Lett.* 19 (6) (2019) 3505–3518.
- [24] W. Zhang, X. Hu, Q. Shen, D. Xing, Mitochondria-specific drug release and reactive oxygen species burst induced by polyprodrug nanoreactors can enhance chemotherapy, *Nat. Commun.* 10 (1) (2019) 1704.
- [25] L. Gong, W. Ding, Y. Chen, K. Yu, C. Guo, B. Zhou, Inhibition of mitochondrial ATP synthesis and regulation of oxidative stress based on {SbW8 O30 } determined by single-cell proteomics analysis, *Angew Chem. Int. Ed. Engl.* 60 (15) (2021) 8344–8351.
- [26] C. Liang, X. Zhang, M. Yang, X. Dong, Recent progress in ferroptosis inducers for cancer therapy, *Adv. Mater.* 31 (51) (2019), e1904197.
- [27] M.L. Steele, S. Fuller, M. Patel, C. Kersaitis, L. Ooi, G. Münch, Effect of Nrf2 activators on release of glutathione, cysteinylglycine and homocysteine by human U373 astroglial cells, *Redox Biol.* 1 (1) (2013) 441–445.
- [28] S.J. Dixon, K.M. Lemberg, M.R. Lamprecht, R. Skouta, E.M. Zaitsev, C.E. Gleason, D.N. Patel, A.J. Bauer, A.M. Cantley, W.S. Yang, B. Morrison 3rd, B.R. Stockwell, Ferroptosis: an iron-dependent form of nonapoptotic cell death, *Cell* 149 (5) (2012) 1060–1072.
- [29] B.R. Stockwell, X. Jiang, W. Gu, Emerging mechanisms and disease relevance of ferroptosis, *Trends Cell Biol.* 30 (6) (2020) 478–490.
- [30] Z. Chen, Y. Peng, Y. Li, X. Xie, X. Wei, G. Yang, H. Zhang, N. Li, T. Li, X. Qin, S. Li, C. Wu, F. You, H. Yang, Y. Liu, Aptamer-dendrimer functionalized magnetic nano-octahedrons: theranostic drug/gene delivery platform for near-infrared/magnetic resonance imaging-guided magnetochemotherapy, *ACS Nano* 15 (10) (2021) 16683–16696.